ORNL/SPR-2023/3132

Advanced Multiscale Microscopy Characterization of High Burnup LWR UO_2 Before and After LOCA Testing

Nuclear Technology Research and Development

Prepared for the US Department of Energy
Advanced Fuels Campaign
Casey McKinney, Chad Parish, Jesse Werden, Tyler Gerczak, Jason Harp, Lauryn Reyes, Nathan Capps
September 30th 2023
M3FT-23OR020204052

SUMMARY

Previous microscopy work within the campaign has observed increased porosity coupled with subgrain formation in the mid-radial region of the fuel. However, examinations of high burnup fuel taken from multiple reactors with different operating conditions have shown that this structure can move radially inward depending on the fuel operating conditions. It is currently theorized that inter- and intragranular fission gas bubble nucleation is precursory to the grain subdivision observed in the mid-radial and central regions of the fuel. Characterization of samples after loss-of-coolant accident (LOCA) testing has revealed that these restructured regions with a high density of bubbles and subgrains pulverize during the transient test. It appears that the increase in fission gas bubbles coupled with grain subdivision renders the fuel mechanically weaker during a LOCA transient and thus susceptible to fuel fragmentation relocation and dispersal (FFRD). Work this past fiscal year has prioritized understanding this behavior by using advanced microscopy to investigate fission gas behavior in the as-irradiated and post-LOCA state. Additional work has been performed to verify the theory described above by analyzing multiple post-LOCA optical micrographs and comparing that to as-irradiated microstructural data. This document reports progress in the post-irradiation characterization of high burnup nuclear fuel with emphasis on the restructured fuel regions, particularly how microstructural features influence FFRD and fission gas release behavior in LOCA conditions.

This page is intentionally left blank.

CONTENTS

SUMMARY iii

FIGURES vii

TABLES viii

ABBREVIATIONS ix

1. INTRODUCTION 1

2. EXPERIMENTAL OBSERVATIONS 2
   - 2.1 Sample Information 2
   - 2.2 Dark Zone Fragmentation Behavior by Optical Microscopy 3
   - 2.3 Nanostructural Features by Scanning Transmission Electron Microscopy 4
     - 2.3.1 Experimental 4
     - 2.3.2 Fission Gas Bubble Evaluations 4
     - 2.3.3 As-Irradiated and Post-LOCA Comparisons 9
     - 2.3.4 North Anna 2 As-Irradiated Analyses 18
     - 2.3.5 Bubble Pressures 21

3. DISCUSSION 22

4. FUTURE WORK 23
   - 4.1 Radial Distribution of Elements Observed by Energy Dispersive X-ray Spectroscopy 23
   - 4.2 Isotopic Characterization by Time-of-Flight Secondary Ion Mass Spectrometry 25

5. SUMMARY 28

6. ACKNOWLEDGMENTS 28

7. REFERENCES 29

This page is intentionally left blank.

FIGURES

Figure 1: OM micrographs capturing the fuel cross-sections of as-irradiated and post-LOCA tested segments from the NA1 and HBR1 rods. 3

Figure 2: Color-mix quantified X-ray map of the five metals (yellow or blue) and Xe (red) from NA1, $r/r_0 \sim 0.13$. 5

Figure 3: Five-metal particles analyzed by hand (left) and by machine vision (right). 6

Figure 4: (a) and (b) show two FGBs from the data in Figure 2 and Figure 3. The left column is a detail of the particle using the centroid and radius estimate from LoG. The second column is the histogram marked with Otsu's threshold (vertical line). The third column shows the bubble as determined by Otsu's threshold. The fourth and fifth columns show the particle as determined by thresholding followed by morphological opening with 1- or 2-pixel radius kernels. The right (last) column shows the bubble and its surroundings. The bottom image (c) shows each of the identified bubbles in a different color. 7

Figure 5: (a) histogram of the FGB equivalent diameters with N_v calculated from an assumed foil thickness of 150 nm. (b) CVF of the FGBs based on an equivalent sphere volume assumption. 9

Figure 6: Comparisons of as-irradiated and post-LOCA tested samples at approximately the same radial distance, ~0.55 r/r_0. The X-ray maps are computed as weight percent with 3 × 3 or 5 × 5 moving averaging before quantification. Regions of vacuum (i.e., panel *f*, top-right corner) are non-physically noisy due to zero count rates. 11

Figure 7: Comparisons of as-irradiated and post-LOCA tested samples at approximately the same radial distance, ~0.53 r/r_0. The X-ray maps are computed as weight percent with 3 × 3 or 5 × 5 moving averaging before quantification. Regions of vacuum (i.e., panel *f* center) are non-physically noisy due to zero count rates. 13

Figure 8: Comparisons of as-irradiated and post-LOCA tested samples at approximately the same radial distance, ~0.77 r/r_0. The X-ray maps are computed as weight percent with 3 × 3 or 5 × 5 moving averaging before quantification. Regions of vacuum (i.e., panel *f*, top-left corner) are non-physically noisy due to zero count rates. 15

Figure 9: Comparison of NA1 as-irradiated and post-LOCA FGB sizes at similar radial positions. Vertical lines are the median. 17

Figure 10: Comparison of NA1 as-irradiated and post-LOCA FGB CVF at similar radial positions, calculated assuming spherical bubbles. Vertical lines are the median. The shape of the curves indicate most of the volume is in the few largest bubbles, especially in post-LOCA 0.51 r/r_0 18

Figure 11: Montage of microstructures from different radial positions in the NA2 as-irradiated samples. 19

Figure 12: EDS maps of all major or secondary elements, quantified in weight percent, from two regions of the same FIB lamella (NA2, as-irradiated, 0.88 r/r_0)..... 20

Figure 13: As-irradiated and post-LOCA bubble pressure estimates for the NA1 0.57 r/r_0 conditions. Note the very high bubble pressures (very small diameters) in the maps are non-physical and removed from the scatterplots. 22

Figure 14: EDS data for different elements at different radial locations in the NA1 as-irradiated sample 25

Figure 15: ToF-SIMS spectra obtained from the HBS in the NA1 as-irradiated sample. (a) Provides the entire spectra collected from 0–300 m/Q. (b)–(e) Show portions of the spectra to highlight the distribution of the individual peaks. 27

TABLES

Table 1: Operating and test conditions for fuel rods available to this project. 2

ABBREVIATIONS

CVF	cumulative volume fraction
EBSD	electron backscatter diffraction
EDS	energy dispersive X-ray spectroscopy
EELS	electron energy loss spectroscopy
EFTEM	energy filtered transmission electron microscopy
EPMA	electron probe microanalysis
FFRD	fuel fragmentation relocation and dispersal
FGB	fission gas bubble
FGR	fission gas release
FIB	focused ion beam
FMP	five-metal precipitate
HAADF	high-angle annular dark field
HAGB	high-angle grain boundary
HBFF	high burnup fuel fragmentation
HBR1	H. B. Robinson 1
HBS	high burnup structure
LAGB	low-angle grain boundary
LOCA	loss-of-coolant accident
LoG	Laplacian of Gaussian
LWR	light-water reactor
MAADF	medium-angle annular dark field
NA1	North Anna 1
NA2	North Anna 2
OM	optical microscopy
ORNL	Oak Ridge National Laboratory
PWR	pressurized water reactor
SEM	scanning electron microscope/microscopy
S/TEM	scanning/transmission electron microscopy
ToF-SIMS	time-of-flight secondary ion mass spectrometry
XSI	X-ray spectrum imaging

ADVANCED MULTISCALE MICROSCOPY CHARACTERIZATION OF HIGH BURNUP LWR UO_2 BEFORE AND AFTER LOCA TESTING

1. INTRODUCTION

Loss-of-coolant accident (LOCA) tests performed at the Halden Boiling Water Reactor showed significant fine fragmentation in high burnup fuel such that some of the fuel was reduced to a sand-like consistency [1-5]. This phenomenon, designated as high burnup fuel fragmentation (HBFF), raised concerns of fuel fragments relocating into the ballooned region of the cladding and possible dispersal from the cladding through the rupture opening, collectively known as fuel fragmentation relocation and dispersal (FFRD). Although the burnup for the fuel from the Halden tests was above 80 GWd/tU, subsequent high burnup LOCA experimental programs have found the burnup threshold for HBFF to be closer to 62 GWd/tU pellet average [6]. Considering the current discharge limit for commercial fuel is 62 GWd/tU (rod average) and the industries desire to extend the burnup beyond 62 GWd/tU (rod average), the mechanisms responsible for HBFF must be understood so that possible mitigating solutions can be derived. One way to achieve this is by utilizing advanced microscopy techniques to characterize the as-irradiated fuel samples prior to LOCA testing to uncover microstructural features that may render the fuel prone to HBFF.

Previous efforts leveraged advanced microscopy techniques to characterize the radial variations in the porosity, grain structure, and five-metal precipitate (FMP) distribution of two high burnup rods from the North Anna pressurized water reactor (PWR) in the as irradiated state and after LOCA testing [7-9]. The porosity and grain structure characterization—obtained from scanning electron microscopy (SEM) and electron backscatter diffraction (EBSD), respectively—indicated regions with high porosity and a high density of grain (and subgrain) boundaries fragmented under LOCA conditions. In the outer regions of the fuel pellet, the high porosity and high concentration of high-angle grain boundaries (HAGB, >15° misorientation) in the high burnup structure (HBS) pulverized during the LOCA tests. In the mid-radial to central regions of the fuel pellet ($0.5 > r/r_0 > 0.3$), high porosity and high concentrations of low-angle grain boundaries (LAGB, <15° misorientation) indicated that restructuring of the microstructure occurred in this region. This restructuring in the central region of the fuel pellets (also referred to as dark zone) pulverized when subjected to a LOCA transient. The onset of this central restructured region also coincided with the appearance of FMPs in the region. While the mechanisms responsible for the formation of the HBS are well understood, the underlying mechanisms behind the formation of the dark zone in the fuel center, which is also prone to HBFF like the HBS, are less clear. Since the burnup profile is known to be flat across the central portion of the fuel radius, the mechanism responsible for the formation of the restructured region in the fuel center is believed to depend on the local temperature and perhaps the temperature gradient. In addition to the SEM analysis, scanning/transmission electron microscopy (S/TEM) analysis was also conducted on one of the as-irradiated North Anna samples [8]. The S/TEM analysis found FMPs present in all liftouts taken from various radial locations with no apparent trend with respect to distance from the cladding. Xenon bubbles were distributed non-uniformly, but often at or near grain boundaries.

Additional S/TEM analysis is needed on samples before and after LOCA testing to obtain a better understanding of what is occurring at the nanoscale during transient testing.

In this work, the results from additional S/TEM characterization are presented. The results from the as-irradiated sample from the second North Anna rod will be discussed along with the results from the analysis of the LOCA tested North Anna 1 (NA1) sample. In the microstructural comparison between the as-irradiated and post-LOCA samples presented in earlier reports, there were no observable microstructural differences between the samples before and after LOCA testing, apart from the significant fragmentation [7, 8]. The S/TEM results in this work will show observable changes that occur at the nanoscale during the transient testing, which can aid in understanding what is driving HBFF. In addition to the S/TEM results, this work will also present the optical microscopy (OM) characterization of a third sample of high burnup LOCA-tested light-water reactor (LWR) UO_2 from the H. B. Robinson PWR. In another work, the radial variations in the porosity and grain structure were characterized for this sample [10]. The H. B. Robinson (HBR1) sample also has a dark zone in the fuel center, but its extent differs from that observed in the North Anna samples due to the different power histories. This will allow for a better understanding of how varied power histories can affect HBFF behavior.

2. EXPERIMENTAL OBSERVATIONS

2.1 Sample Information

In this work, the multiscale microscopy characterization of three high burnup commercial LWR UO_2 samples is presented. The OM, SEM, and partial TEM results for the North Anna samples were previously provided in earlier reports [7, 8]. This work will build on the previous characterization efforts and provide more detailed TEM results for the NA1 as-irradiated sample, NA1 post-LOCA sample, and North Anna 2 (NA2) as-irradiated sample. In addition to the results from the North Anna samples, the OM characterization of the HBR1 before and after LOCA testing will be discussed. In Table 1, the operating histories and test conditions for the rods examined in this work are given. The HBR1 sample was run at a lower last cycle power compared to the North Anna samples. The objective of this work is to determine how the dissimilar power histories affect the evolution of the microstructure and consequently the fragmentation behavior.

Table 1: Operating and test conditions for fuel rods available to this project.

Sample	Father rod burnup (GWd/tU)	Sample burnup (GWd/tU)	Last cycle power (kW/m)	LOCA test	LOCA heating rate (°C/s)	Terminal temperature (°C)	Mass fraction < 1 mm (%)	Ref.
NA1	63	69	19–23	Yes	5	1200	27.4	[11]
NA2	68.5	77	19–23	Yes	5	1000	25.2	[11]
HBR1	66.5	71	10–5	Yes	5	1000	31.59	[11]

2.2 Dark Zone Fragmentation Behavior by Optical Microscopy

In Figure 1, the cross-sections of the as-irradiated and post-LOCA tested segments from the NA1 and HBR1 rods are shown. In the top half of the figure capturing the NA1 rod, the dark zone can be seen as a ring around the center of the pellet in the as-irradiated sample. The previous SEM and EBSD characterization of this sample notes that the dark zone is a region with high porosity and high concentrations of LAGBs [8, 9]. This indicates the presence of local restructuring of the microstructure. The post-LOCA micrograph for the NA1 sample shows large cracking throughout this dark zone, suggesting that this microstructure in particular is susceptible to extensive fragmentation.

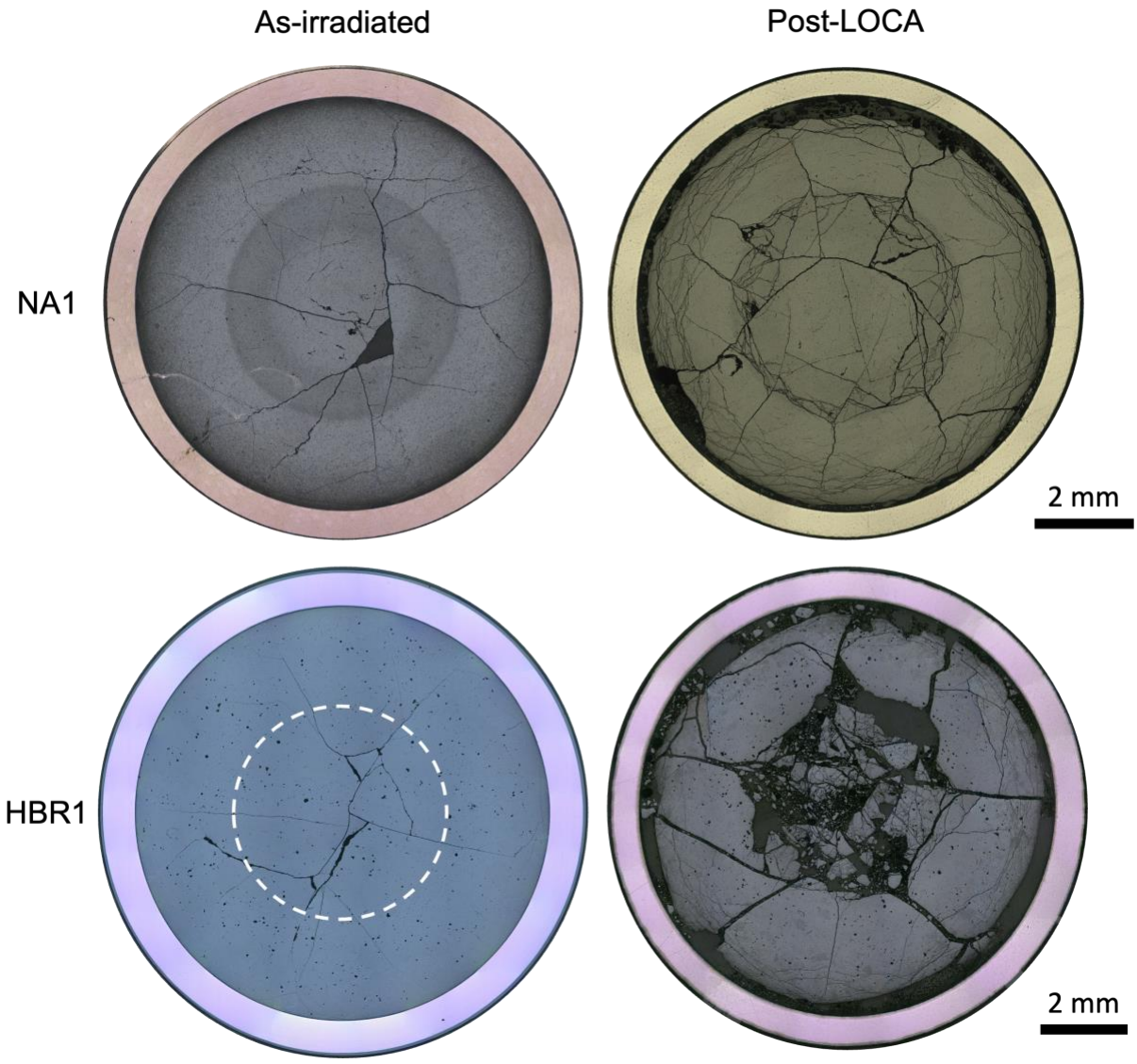

Figure 1: OM micrographs capturing the fuel cross-sections of as-irradiated and post-LOCA tested segments from the NA1 and HBR1 rods.

A white dotted circle has been added to the bottom left-hand micrograph in Figure 1. This circle denotes where the dark zone appears in the sample. Although the contrast between the different zones of the fuel is not as apparent in the HBR1 as-irradiated sample, higher magnification darkfield images were collected to verify the light–dark zone transition. Additionally, previous EBSD characterization confirms that the dark zone in the HBR1 sample shows increased porosity and subgrain formation similar to the structures observed in the central transition region (dark zone) of the North Anna samples. Unlike the North Anna samples, the H. B. Robinson dark zone appears to propagate to the center of the fuel, whereas the dark zone region in the North Anna samples was a ring with a clean central region. The OM micrograph from the LOCA tested HBR1 rod segment shows significant fragmentation in the entire center of the fuel pellet. This is in contrast to the NA1 sample, which experienced significant fragmentation in the dark zone ring and did not propagate to the center of the fuel pellet. This variation in the microstructural progression affects the fragmentation behavior, as can be seen by the differences in the post-LOCA OM micrographs. The difference in the extent of the dark zone in the two samples is likely a result of their dissimilar power histories, further highlighting the need to understand the effect of operational conditions on microstructure evolution and ultimately HBFF.

2.3 Nanostructural Features by Scanning Transmission Electron Microscopy

2.3.1 Experimental

Focused ion beam (FIB) methods were used to produce liftout lamellas from different radial locations in the high burnup fuel specimens. During this work, as-irradiated and post-LOCA high burnup samples were prepared by FIB and then examined by S/TEM.

The primary goal of the S/TEM work is to first characterize the fission gas bubble (FGB) distributions, and second to compare the as-irradiated and post-LOCA FGB distributions.

The FIB samples were examined in the Oak Ridge National Laboratory (ORNL) Talos F200X S/TEM tool operated at 200 kV and ~0.5-2 nA probe current. STEM imaging was used to evaluate the grain structures, FMP, and FGB structures. Furthermore, X-ray spectrum imaging (XSI) via energy dispersive X-ray spectroscopy (EDS) was used to characterize the structures. Specifically, intragranular and grain boundary regions were examined by XSI methods to determine the distributions of FGBs and FMPs in relation to each other, grain boundaries, bubbles, and other microstructural features. Typical FIB foils contained multiple UO_2 grains and large open regions that were probably large (micron-scale) prior-FGBs that were depressurized by the FIB.

2.3.2 Fission Gas Bubble Evaluations

The first analysis characterizes the distributions of FGBs (and FMPs) in the samples. No krypton was observed; the bubbles are pure xenon to the resolution of EDS (probably ~1 wt % or so). Bubbles are most effectively visualized by using the quantification routines in Thermo Scientific Velox software, which peak-fits the Xe L-series and U M-series X-rays to remove background and overlap effects. All images herein are from a weight fraction quantification to suppress background effects and sharpen the xenon contrast.

An example of the evaluation method is presented in Figure 2 and Figure 3 from NA1 as-irradiated, $r/r_0 \sim 0.13$. In Figure 2, a false-color map image of the five metals (Mo, Tc, and Ru in yellow, and Rh and Pd in blue) and Xe (red) is given. Both small (a few nanometers) and large (tens of nanometers) FGBs and FMPs are present. In Figure 3, the left image shows FMPs analyzed by a human analyst using ImageJ software; this took 5–10 minutes. The right image uses the Laplacian of Gaussian (LoG) approach, implemented in Python using scikit-image, to find the FMPs and required ~5–10 seconds. For crisp high-signal datasets such as these, the machine vision and human analysis agree almost perfectly (discounting effects such as particles cutting the edge of the image and being ignored as incomplete).

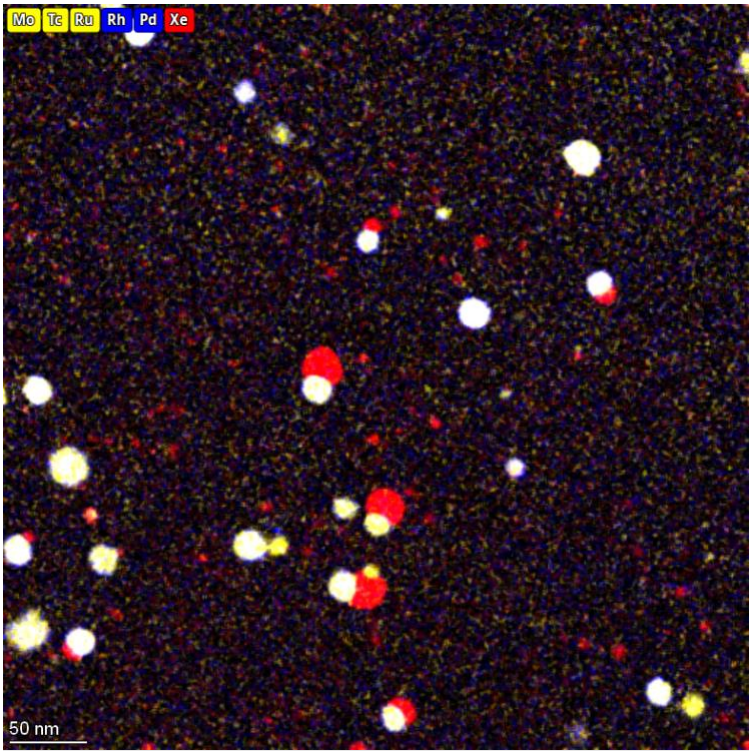

Figure 2: Color-mix quantified X-ray map of the five metals (yellow or blue) and Xe (red) from NA1, $r/r_0 \sim 0.13$.

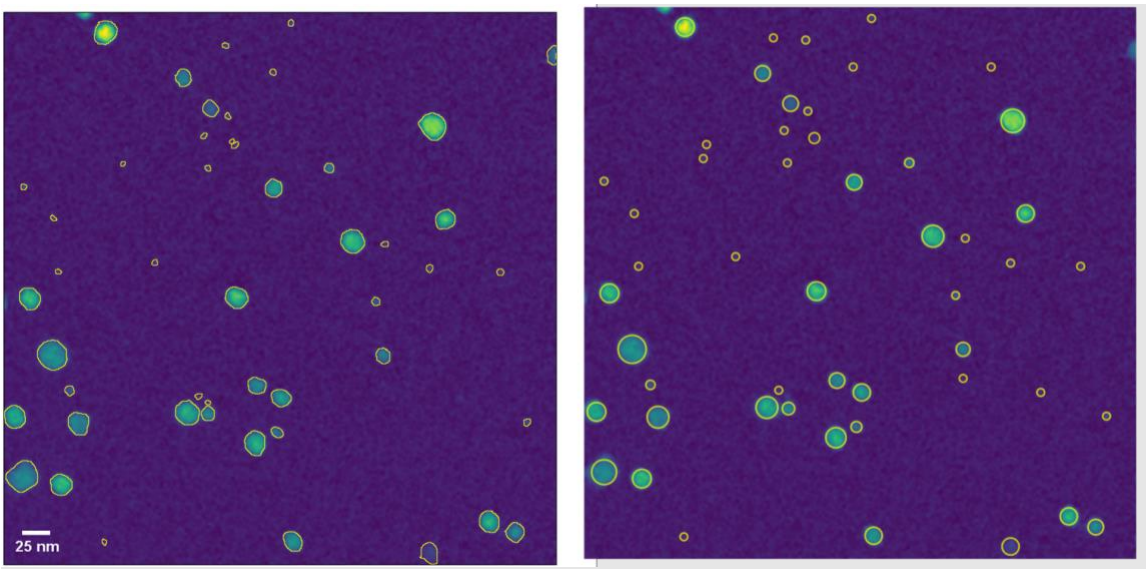

Figure 3: Five-metal particles analyzed by hand (left) and by machine vision (right).

From the LoG approach, particle centroids and approximate sizes are found. However, the sizes from the algorithm are not precise enough for sizing the FGBs or FMPs, so a refinement analysis is performed on each discovered particle. Two examples are given: Figure 4(a)–(b). The first (left) column of each shows a detail of the area around the FGB as determined by the centroid and radius estimated from the LoG machine vision calculation. A histogram of the pixel values is given in the second column, with a vertical line denoting the threshold value to separate foreground from background as determined by Otsu's criterion. The third column shows the thresholded bubble.

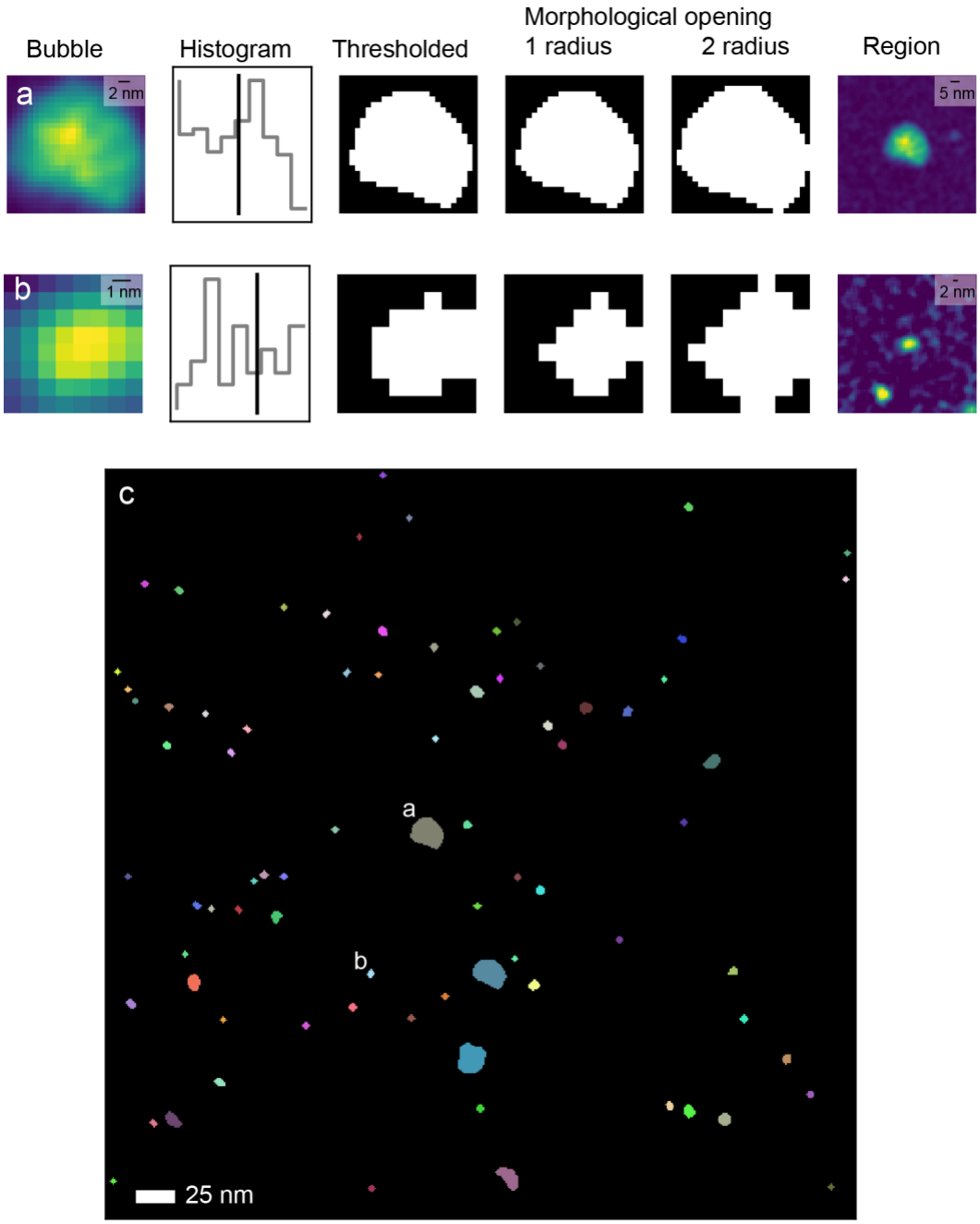

Figure 4: (a) and (b) show two FGBs from the data in Figure 2 and Figure 3. The left column is a detail of the particle using the centroid and radius estimate from LoG. The second column is the histogram marked with Otsu's threshold (vertical line). The third column shows the bubble as determined by Otsu's threshold. The fourth and fifth columns show the particle as determined by thresholding followed by morphological opening with 1- or 2-pixel radius kernels. The right (last) column shows the bubble and its surroundings. The bottom image (c) shows each of the identified bubbles in a different color.

Thresholding can provide very noisy results; therefore, morphological opening is used to clean the edges of the thresholded bubbles. In particular, this helps remove isolated pixels of noise while leaving the center of a bubble untouched and smoothing the edges into a more physically reasonable form. Opening is an image processing method in which the thresholded image is eroded by a given kernel, and then the eroded image is dilated by the same kernel, smoothing the edges and removing isolated pixels.

For a large (several-pixel-radius) bubble, such as the top row (Figure 4(a)), the opening process and the radius of the kernel make little difference. For a smaller bubble (bottom row, Figure 4(b)), the pixels along the edge can be somewhat smoother for the larger kernel. Another effect is that the smallest bubbles (1–2 pixels in radius) are eliminated by this opening, which is beneficial to ensure that artifacts that are pure noise rather than actual FGBs are eliminated. This could, however, bias the data by removing the very smallest bubbles that are at the noise floor.

From these operations, each individual bubble is estimated based on the contrast of the fission gas in the quantified XSI. Equivalent diameters are calculated from the area and the individual pixel size (either pixel edge in nanometers or pixel area in square nanometers). The bottom panel, Figure 4(c), shows the result of this analysis, in which each FGB is colored individually. The two bubbles in Figure 4(a) (top row) and Figure 4(b) (second row) are marked *a* and *b* in the figure for direct comparison.

Now that the individual FGBs have been detected and sized, enough information is available to calculate the areal densities and, from knowledge of the local lamella thickness, the number densities. Future work involves using energy filtered TEM (EFTEM) and electron energy loss spectroscopy (EELS) to measure the thickness of the TEM lamellas; however, because the EFTEM system in the irradiated laboratories was down and only recently repaired, this will take place in the future. Presently, assumptions of foil thickness are being used to calculate the number densities of the FGBs in these samples. For an assumption of 150 nm thickness, the number density of FGBs in this dataset is $\sim 2 \times 10^{21}$ m^{-3}. The histogram of FGB sizes vs. density is given in Figure 5(a), and a cumulative volume fraction (CVF, calculated from converting equivalent circular diameters to equivalent spherical volumes) is given in Figure 5(b). The uptick at the high-diameter side of the CVF indicates that the few largest FGBs contain most of the volume.

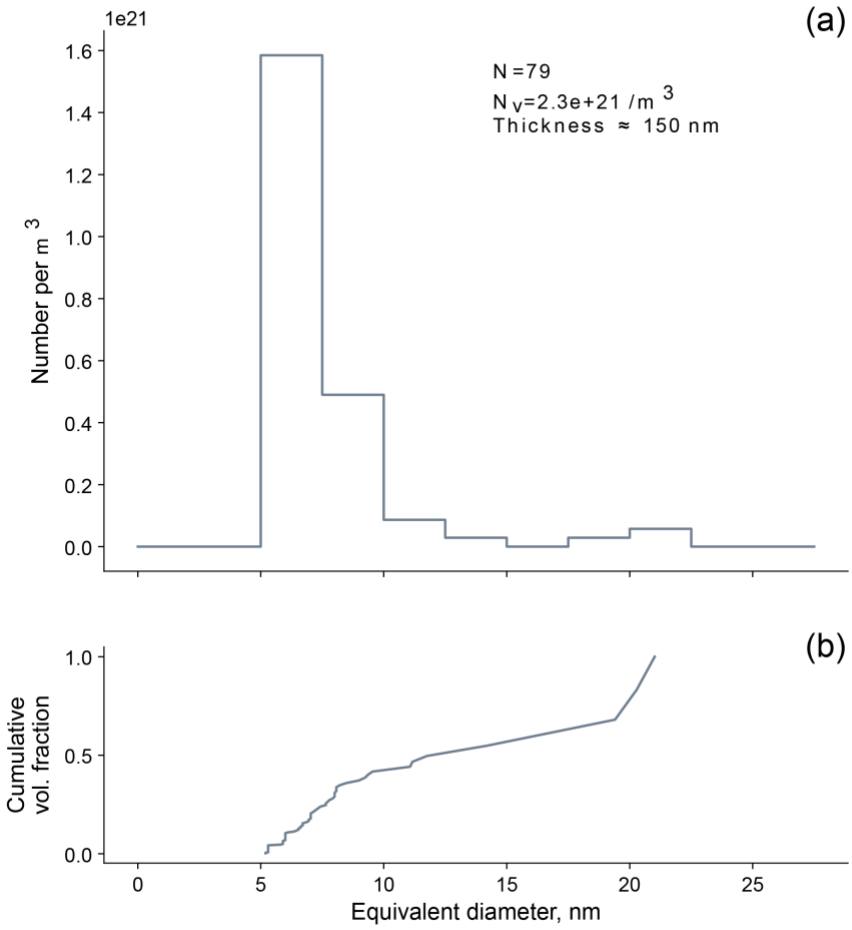

Figure 5: (a) histogram of the FGB equivalent diameters with N_v calculated from an assumed foil thickness of 150 nm. (b) CVF of the FGBs based on an equivalent sphere volume assumption.

The FGBs in this dataset were found to have a median equivalent diameter of 7 nm, a maximum of 21 nm, and a minimum of 5 nm—the minimum bubble size will depend on the foil thickness, but it will likely be around 5 nm in many cases. It is important to note that these are equivalent diameters, not Feret's diameters, so individual chords on individual FGBs may be slightly more than this maximum or slightly less than this minimum due to the non-circularity of the FGBs.

This overall method, therefore, can be utilized to analyze the statistics of the FGBs (or FMPs) in each dataset.

2.3.3 As-Irradiated and Post-LOCA Comparisons

The most important results from the present work are comparisons of as-irradiated and post-LOCA samples from approximately the same radial regions in NA1 and secondarily comparisons with the as-irradiated NA2 samples.

Figure 6 shows the ~0.57 r/r_0 (~1,800 μm from the cladding) region. This region is in the central restructured region (dark zone) near the border with the mid-radial region. In the top row of Figure 6, the general microstructures (as imaged by medium-angle annular dark-field (MAADF)-STEM) are seen. In the as-irradiated samples—NA1 in Figure 6(a) and NA2 in Figure 6(b)—bubbles are seen that were presumably filled with fission gas prior to FIB preparation. Grain boundary cracking is also apparent (red arrow). Several smaller (approximately half a micron) grain boundary or triple point bubbles are also visible (i.e., yellow arrow in the NA1 as-irradiated figure). In the post-LOCA shown in Figure 6(c), similarities and differences are noted. The number of small, high-aspect, lenticular bubbles appears higher, and they seem less associated with the grain boundaries and more intragranular.

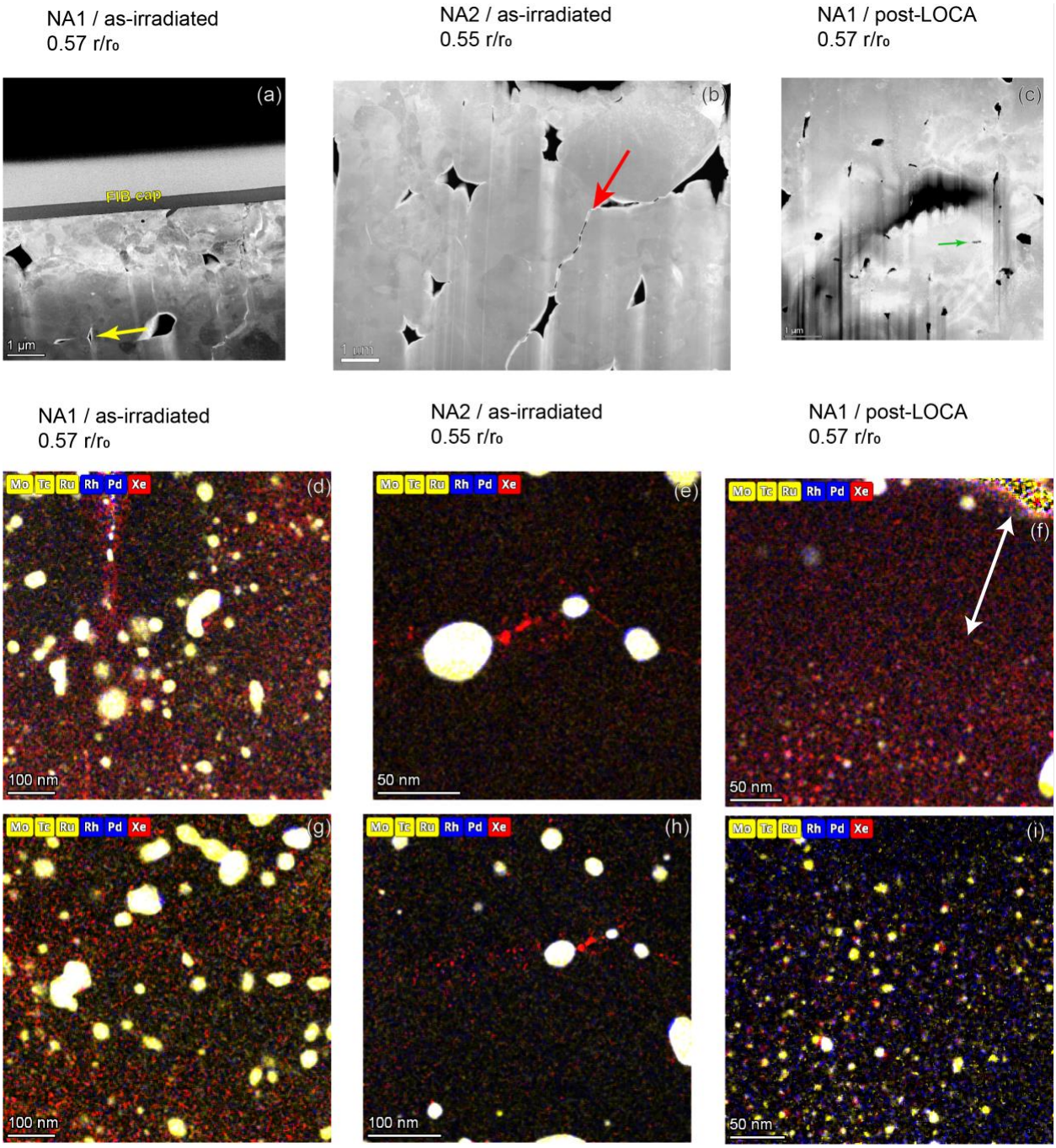

Figure 6: Comparisons of as-irradiated and post-LOCA tested samples at approximately the same radial distance, ~0.55 r/r_0. The X-ray maps are computed as weight percent with 3 × 3 or 5 × 5 moving averaging before quantification. Regions of vacuum (i.e., panel *f*, top-right corner) are non-physically noisy due to zero count rates.

The X-ray mapping of these samples are given in the bottom rows of Figure 6(d)–(i). Densities and sizes of the FMPs differ between the as-irradiated and post-LOCA samples; surprisingly, the

post-LOCA sample shows smaller and more fractionated FMPs. The FGB sizes are similar but polydisperse enough to make by-eye comparisons difficult; quantification will be below.

Perhaps the most important observation is that the small intragranular "tears" present in the post-LOCA appear to have a FGB denuded zone around them. This is visible in Figure 6(f). The top-right corner of Figure 6(f) (which is noisy) is the vacuum in the tear. Surrounding the tear, no FGBs (red xenon map channel) are observed for ~150–200 nm around the tear. Small FGBs manifest 150–200 nm away from the tear. Clearly, more exploration is needed to explain and understand this, but it seems possible that the tear is driven by a bubble being overpressurized by collecting localized fission gas during the LOCA temperature excursion. A white double-headed arrow denotes the approximate denuded zone.

The ~0.53 r/r_0 (~2000–2050 μm) region, slightly closer to the center, shows similar behavior (Figure 7). The post-LOCA NA1 in Figure 7(c) shows significant numbers of the small lenticular tears similar to those seen in Figure 6. Similar to observations in Figure 6, the as-irradiated NA1 in Figure 7(a) and NA2 in Figure 7(b) do not show the same morphology, and the voids in these as-irradiated specimens are more intergranular and polygonal and less intragranular and lenticular.

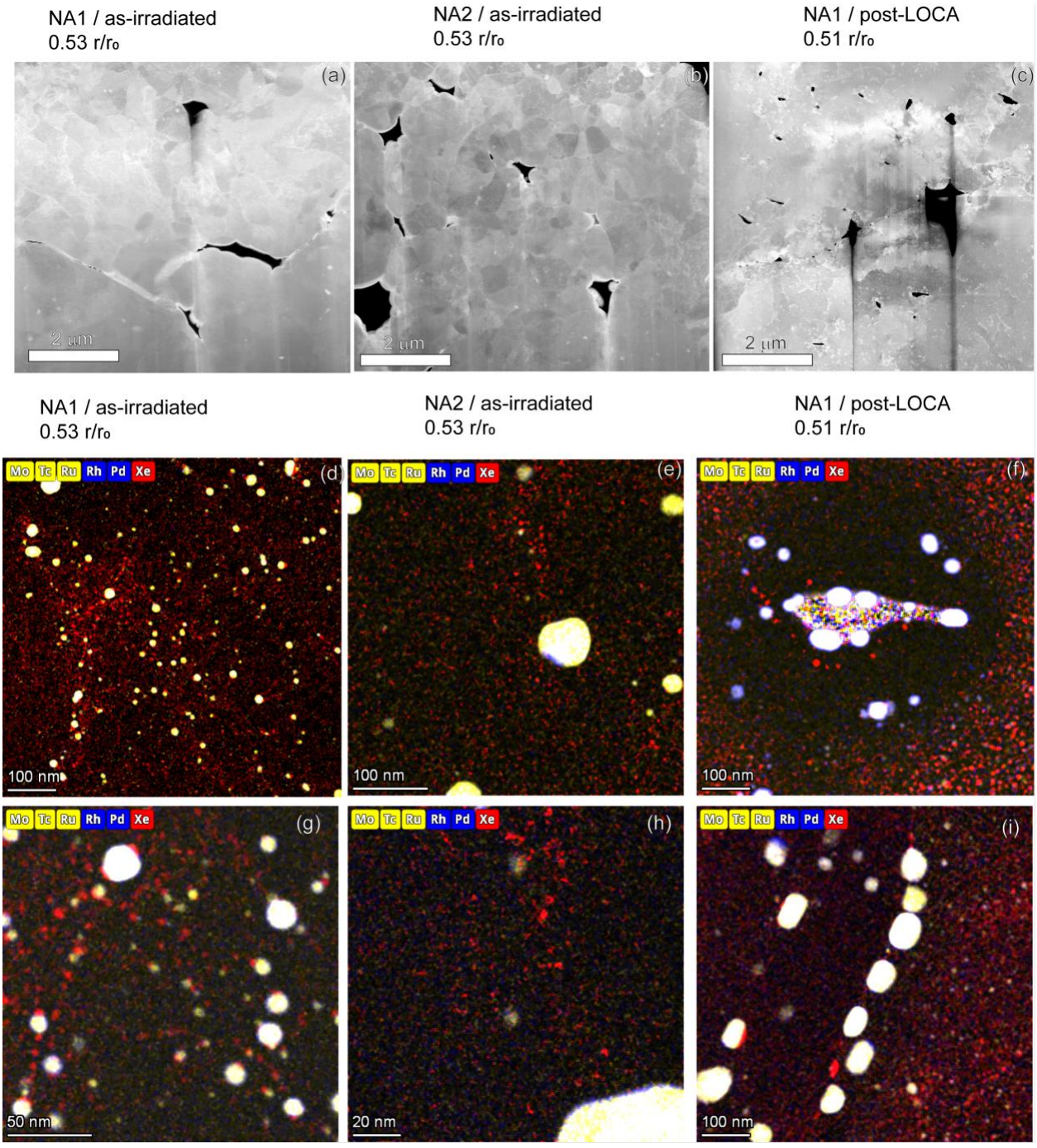

Figure 7: Comparisons of as-irradiated and post-LOCA tested samples at approximately the same radial distance, ~0.53 r/r_0. The X-ray maps are computed as weight percent with 3 × 3 or 5 × 5 moving averaging before quantification. Regions of vacuum (i.e., panel *f* center) are non-physically noisy due to zero count rates.

As above, the FMPs are greatly dissimilar in the three conditions, Figure 7(d)–(i). This once again illustrates the inherent inhomogeneities in the high burnup structures at the local level.

However, one of the lenticular tears in the post-LOCA sample in Figure 7(f) again shows the FGB denuded zone around the tear. The denuded zone extends ~100–200 nm again, as above, but a few sharp FGBs are present near the tear inside the denuded zone. Furthermore, a number of large, rectangular grain boundary FMPs are observed in Figure 7(i) with an FGB denuded zone to the left but not to the right, and large FGBs are present along some of the FMPs, clearly showing the association of the fission gas with the particles and possible coarsening of some of the FGBs under the LOCA conditions.

Once again, very small FGBs were observed to remain in the post-LOCA region, as shown in Figure 7(f) and Figure 7(i).

Closer to the edge of the pellet (~900 μm, ~0.76–79 r/r_0), different behavior is seen in Figure 8. Few or none of the lenticular tears are visible in the post-LOCA sample in Figure 8(c). In the as-irradiated samples shown in Figure 8(a)–(b), small voids are again seen to be mostly intragranular (indicated by an arrow in Figure 8(a)). Furthermore, minor grain boundary cavitation (indicated by red arrows in Figure 8(c)) is observed in the post-LOCA sample.

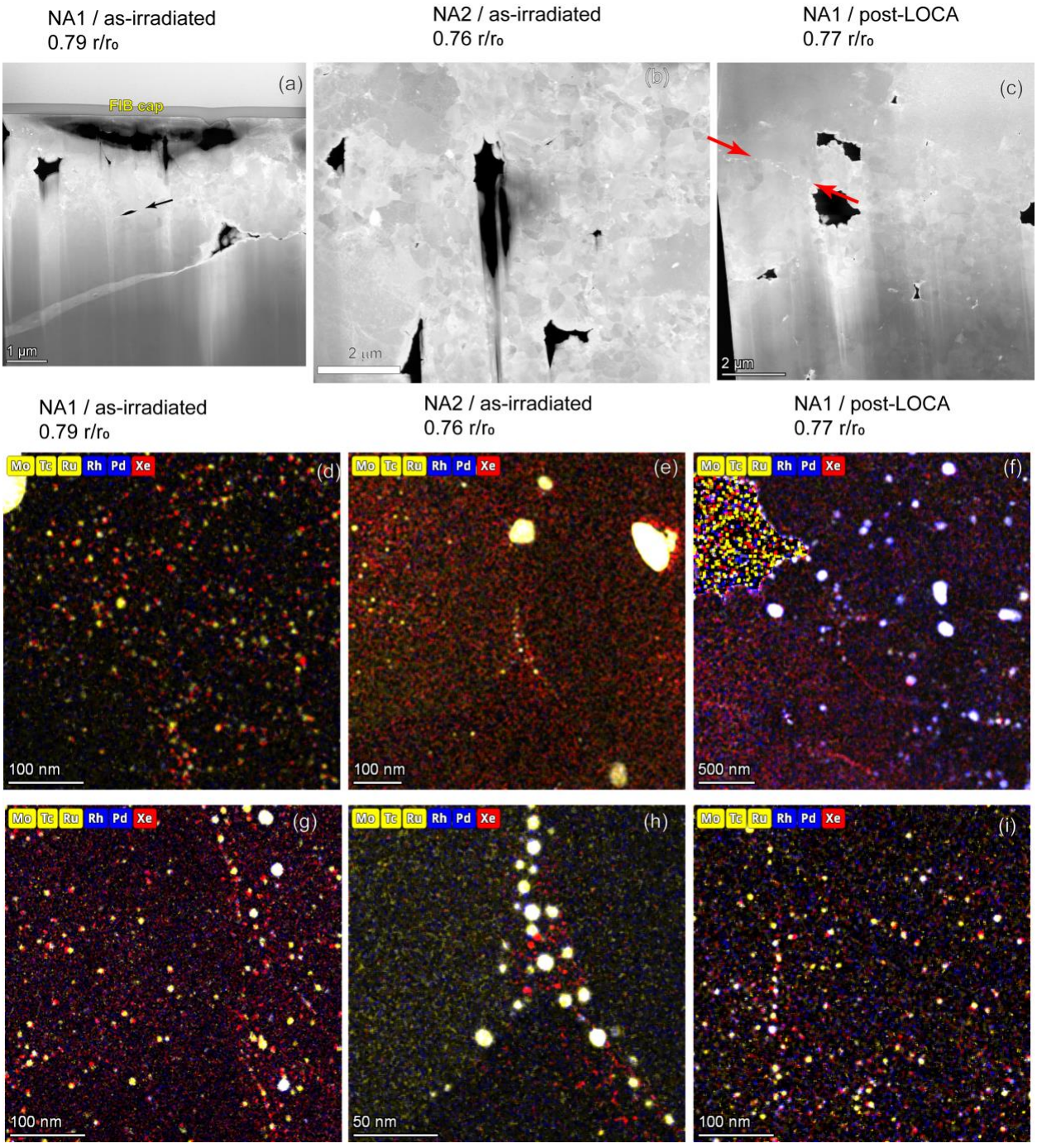

Figure 8: Comparisons of as-irradiated and post-LOCA tested samples at approximately the same radial distance, ~0.77 r/r_0. The X-ray maps are computed as weight percent with 3 × 3 or 5 × 5 moving averaging before quantification. Regions of vacuum (i.e., panel *f*, top-left corner) are non-physically noisy due to zero count rates.

Large and small FMPs are observed in the as-irradiated samples, NA1 (Figure 8(a)) and NA2 (Figure 8(b)). As in the above samples, intragranular and grain boundary FMPs are apparent, and

so are FGBs. Once again, the post-LOCA sample contains many fine FGBs and FMPs, as shown in Figure 8(f) and Figure 8(i), similar to the as-irradiated samples shown in Figure 8(d)–(e) and Figure 8(g)–(h).

Overall, the differences noticeable in the as-irradiated vs. post-LOCA samples here in the ~0.77 r/r_0 region are much less pronounced than the differences in the ~0.55 r/r_0 region in the previous figures. This suggests the mechanism driving pulverization may not be present in this region of the fuel.

As noted above, number densities (FGBs per cubic meter) are necessarily estimates because the foil thicknesses are estimated. Nevertheless, the relative fractions of FGBs of a given size can be compared, acknowledging the absolute fractions are estimates, so here absolute numbers of FGBs are presented in Figure 9. This compares the as-irradiated and post-LOCA NA1 samples at the same (approximate) radial positions as horizontal pairs. Overall, the FGB sizes are generally similar in the as-irradiated and post-LOCA, although the ~0.51 post-LOCA data shows somewhat larger FGBs; this is likely due to the abnormally large FMPs in the same dataset (Figure 7(i)). Overall, the region-to-region variations from one dataset to another in the same specimen/position are generally larger than the sample-to-sample variation, making firm conclusions difficult.

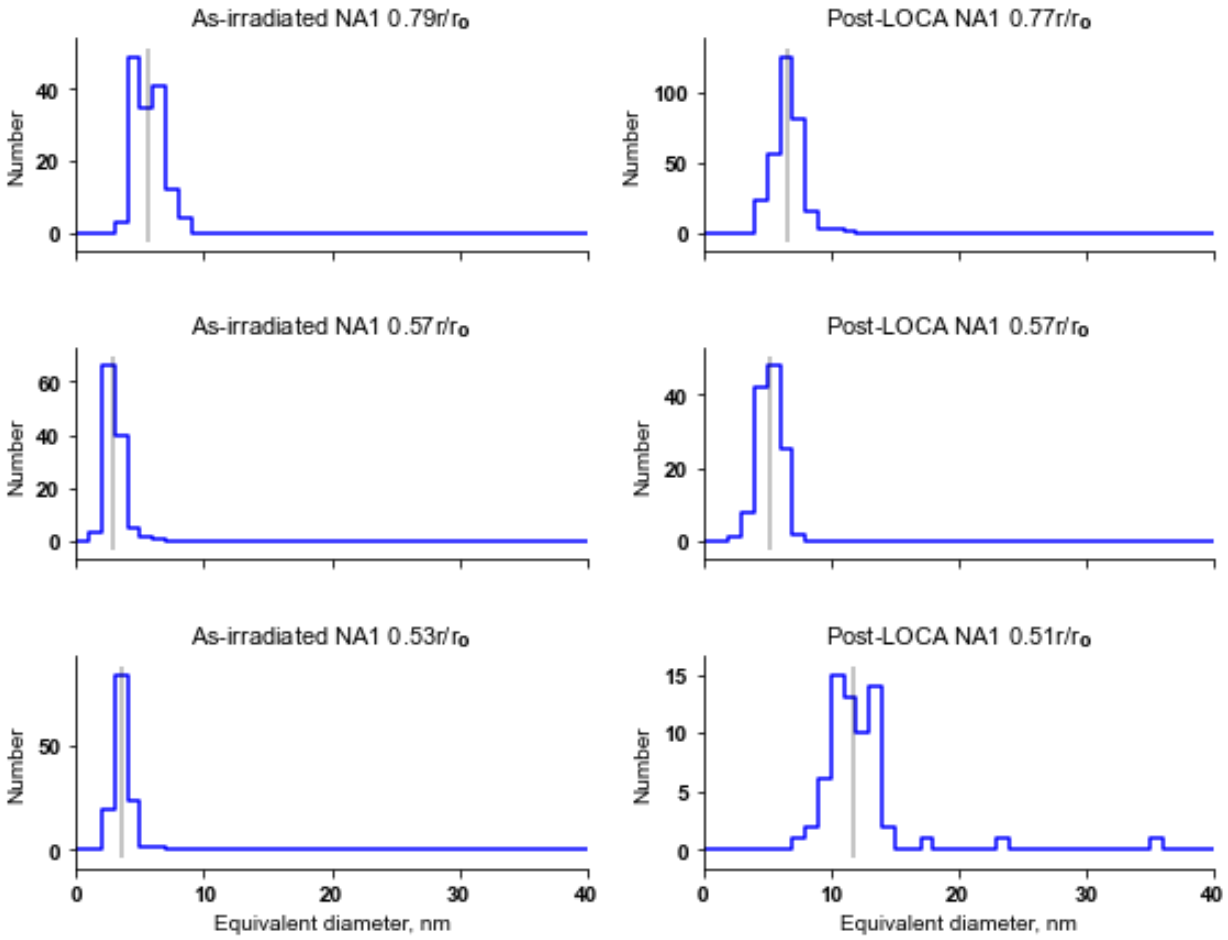

Figure 9: Comparison of NA1 as-irradiated and post-LOCA FGB sizes at similar radial positions. Vertical lines are the median.

Cumulative distribution functions for the equivalent volumes (calculated from the equivalent diameters and assuming sphericity for simplicity) are also calculated, as shown in Figure 10.

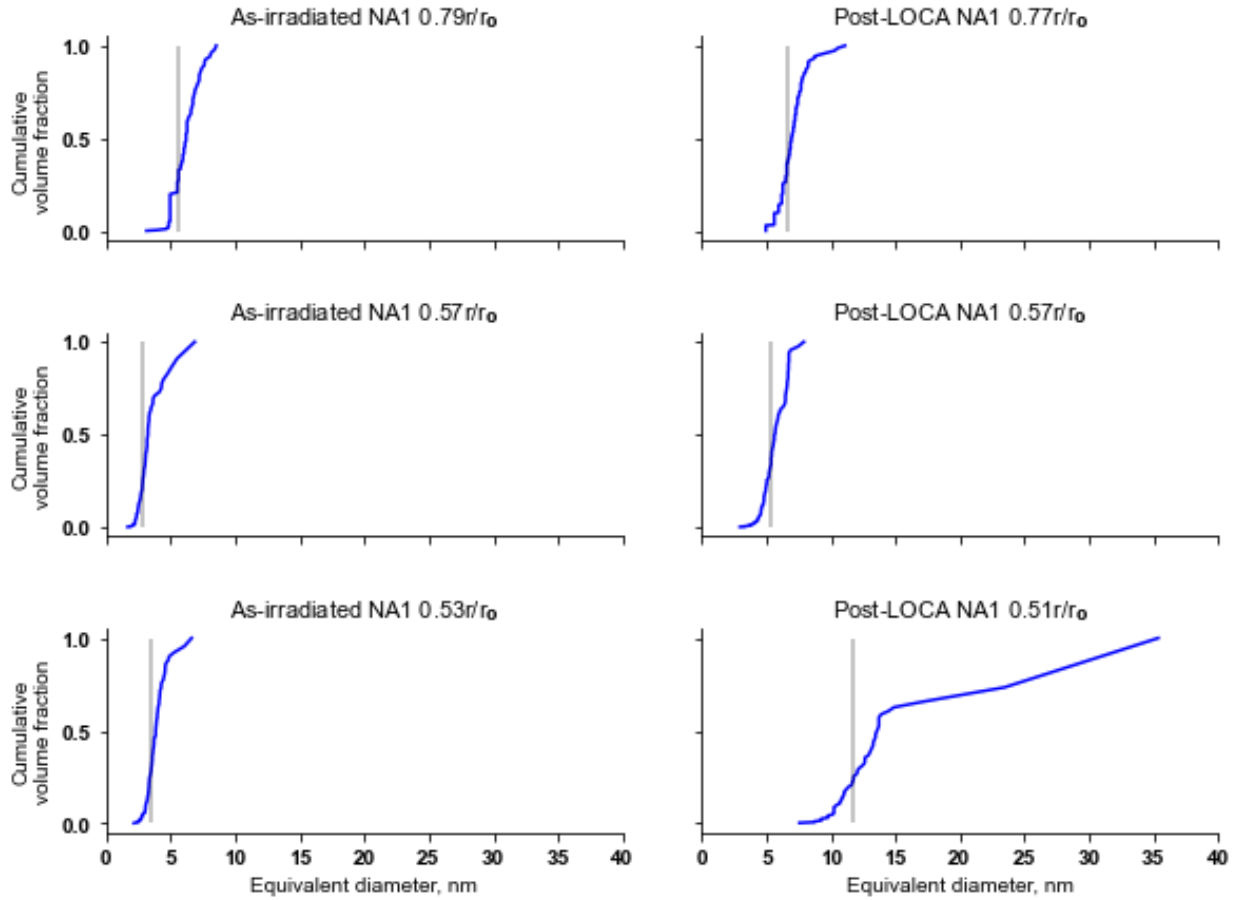

Figure 10: Comparison of NA1 as-irradiated and post-LOCA FGB CVF at similar radial positions, calculated assuming spherical bubbles. Vertical lines are the median. The shape of the curves indicate most of the volume is in the few largest bubbles, especially in post-LOCA 0.51 r/r_0.

2.3.4 North Anna 2 As-Irradiated Analyses

Comprehensive analysis of the through-radial sections of NA2 were performed; typical data is provided in Figure 11. It is, however, worthwhile to note that the individual datasets may be typical but are not representative because all the samples are grossly inhomogeneous from region to region within a single FIB liftout. (See Figure 12 and the discussion below regarding inhomogeneities.) Figure 11 shows individual regions horizontally with the r/r_0 value marked; vertically, the high-angle annular dark field (HAADF), Mo+Tc+Ru, Rh+Pd, and Xe maps are given. (Mo, Tc, and Ru are grouped into a single color because they tend to co-segregate, and Rh+Pd are grouped into a single color because they tend to co-segregate. Xe is the only fission gas measurable in the FGBs. All the maps are the same scale (450 nm square)).

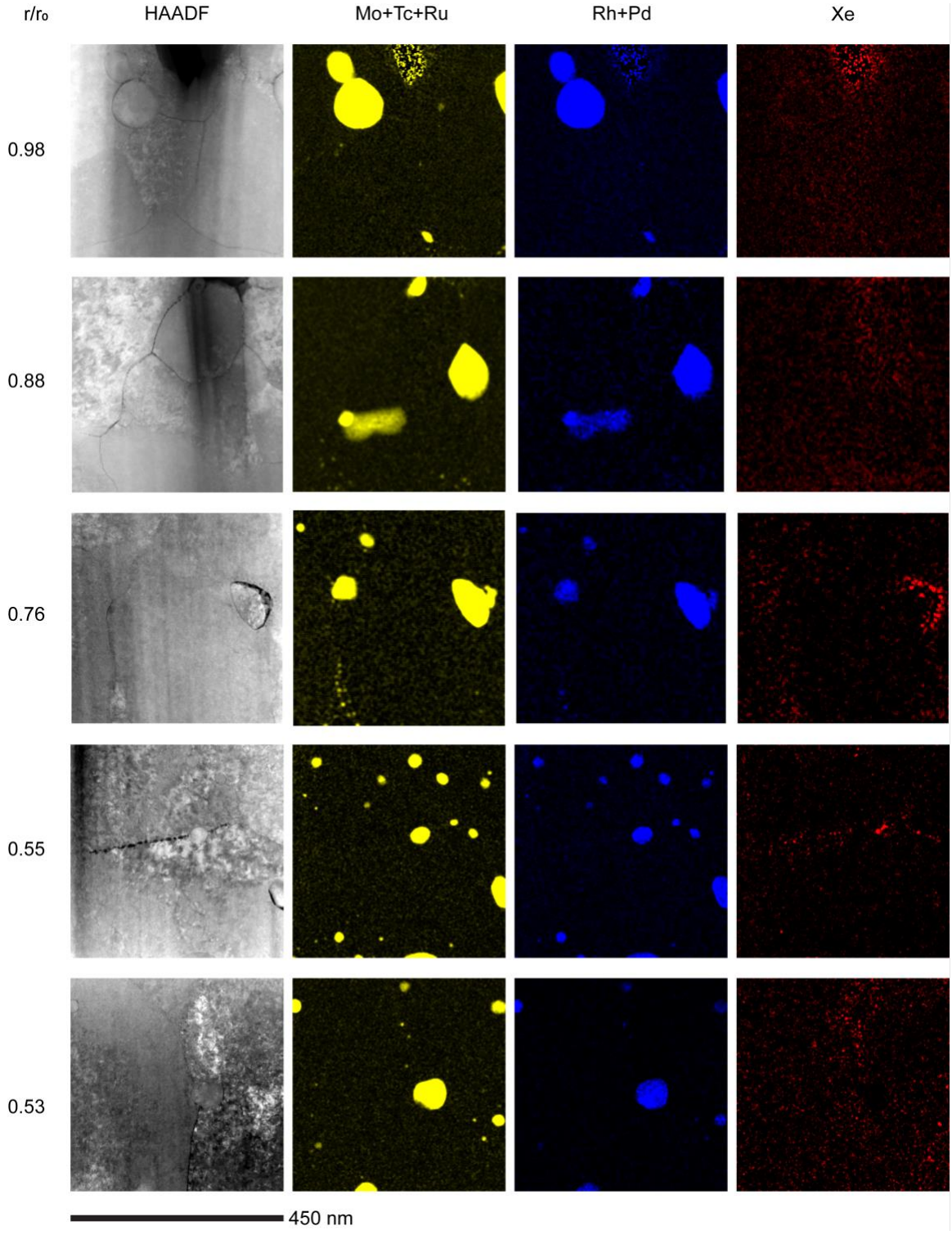

Figure 11: Montage of microstructures from different radial positions in the NA2 as-irradiated samples.

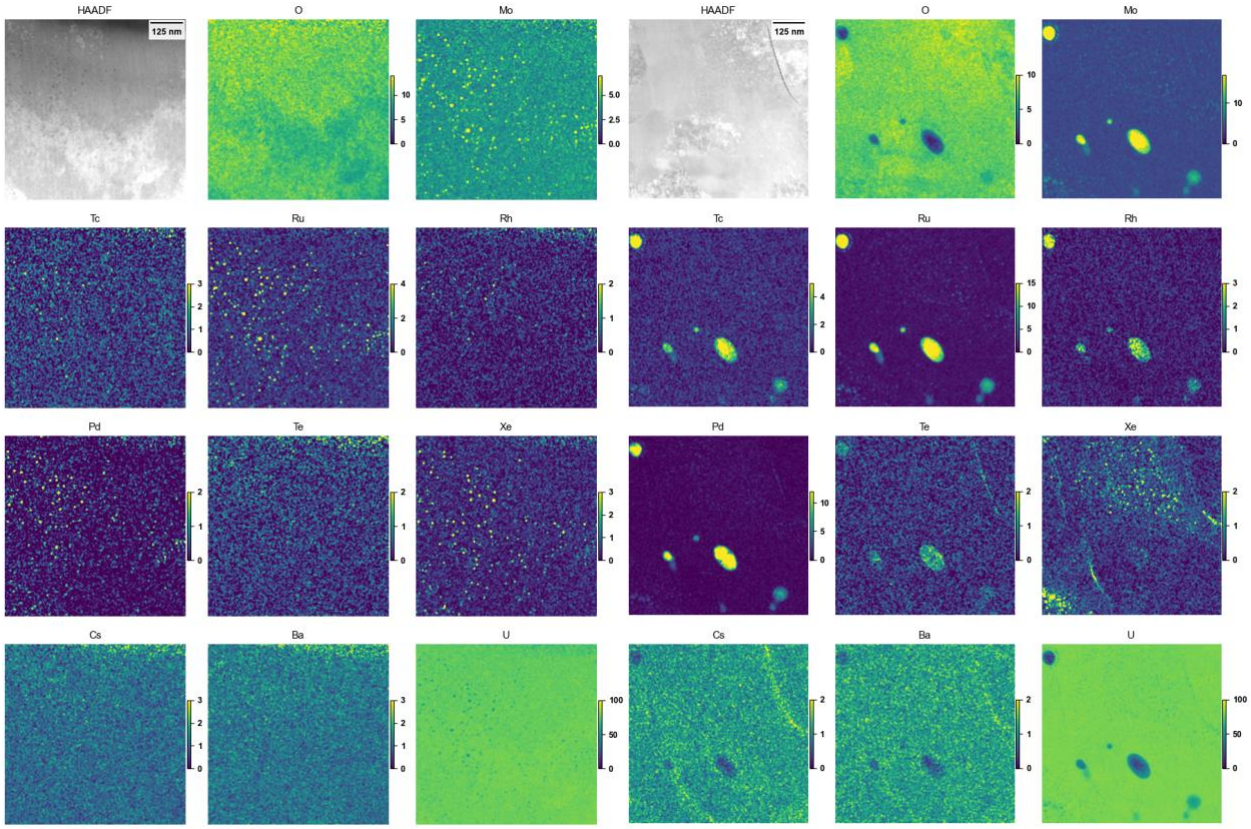

Figure 12: EDS maps of all major or secondary elements, quantified in weight percent, from two regions of the same FIB lamella (NA2, as-irradiated, 0.88 r/r_0).

In Figure 11, all the regions show gross similarities: large and small FMPs and small FGBs. The FGBs on features, such as a large FMP or a grain boundary, are generally larger than the intragranular FGBs that often are attached to fine-scale FMPs. This is particularly pronounced in the 0.76 r/r_0 dataset (Figure 11) in which a large FMP is present on the right side, and very large FGBs decorate the right side of the particle.

In Figure 12, two regions from the sample liftout at 0.88 r/r_0 (~500 μm from the cladding) are presented to illustrate the differences in nearby regions. Both are the same scale (700 nm square), but the features are not similar. These images show individual elemental maps on an absolute colorscale (rather than the qualitative colormixes of Figure 6, etc.) The colorbars are the estimate weight percentage (wt%) of each element, using the vendor algorithm. Note that the areas of vacuum, once again, show noise due to quantifying only noise counts.

The left panel in Figure 12 shows a grain interior with FMPs and associated FGBs, all very fine (a few nanometers to perhaps 15 nm). The right panel, however, shows two grain boundaries, large (hundreds of nanometers) and small (a few nanometers) FMPs, and a wide range of FGB sizes despite both maps being within a few microns of each other in the same FIB liftout, illustrating the differences and polydispersity in all the distributions.

Also interesting, small amounts of minor fission products (Te, Cs, Ba) are observed in the right panel of Figure 12. It is not yet clear whether these are real or an artifact arising from the large

number of overlapping X-ray lines in the 3.5–4.5 keV range, i.e., U M_3–O_5 at ~4.21 keV and U M_1–N_2 at ~4.27 keV possibly interfering with Cs $L\alpha^{12}$ (L_3–M_5) at ~4.28 keV, or such as Pu M_3–N_4 interfering with Te $L\alpha^{12}$. However, because these fission products appear to be more strongly present where the matrix is less strong (i.e., at interfaces or cracks), they require deeper investigation in the future.

2.3.5 Bubble Pressures

Lastly, preliminary bubble pressure comparisons are made. This technique is still being refined and subject to large uncertainties but is worth exploring. As summarized in the previous reports [8, 12], the number of xenon atoms required to produce a measured number of Xe L-series counts is straightforward to calculate; the volume of the bubble can be estimated to produce an estimated volume, and then the atoms per unit volume is found. From the xenon equation of state [13] and the estimated temperature, the pressure in each bubble can be estimated.

This procedure involves multiple inherently noisy inputs (particularly bubble size and X-ray counts) and is therefore expected to have a large uncertainty. The smallest bubbles (with the fewest X-ray counts and most difficult to ascertain diameter) are removed from subsequent calculations to minimize their noise contributions; future work will estimate what fraction of the total Xe is in the smallest bubbles. Specifically, FGBs with fewer than 60 Xe Lα counts and/or less than 2 nm equivalent diameter are discounted as too noisy to analyze.

Nevertheless, estimates of bubble pressures for the as-irradiated and post-LOCA NA1 samples at ~0.57 r/r0 are presented in Figure 13. The top row of Figure 13 shows scatterplots of the estimated pressure vs. 1/r; a priori, a linear dependance is expected. Within the limits of the very noisy data, this trend is present in both. The bottom rows of Figure 13 show the estimated maps (determined from the analyses that yielded Figure 9 and Figure 10).

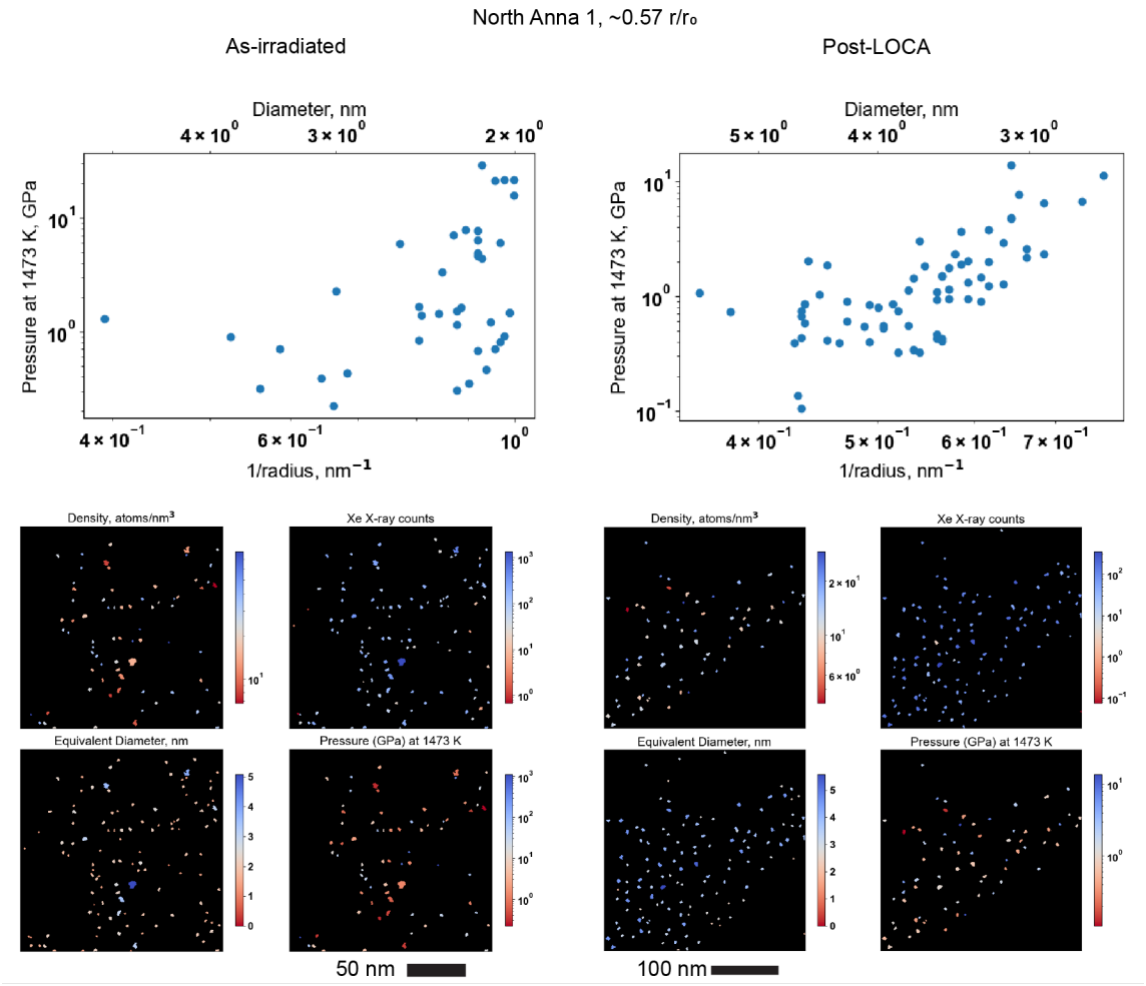

Figure 13: As-irradiated and post-LOCA bubble pressure estimates for the NA1 0.57 r/r_0 conditions. Note the very high bubble pressures (very small diameters) in the maps are non-physical and removed from the scatterplots.

Broadly, bubbles pressures are in the 0.2–20 GPa range, with smaller bubbles having larger estimated pressures. The maps (bottom rows) indicate a few bubbles with unphysically high pressures, ~102–103 GPa. These are universally the smallest bubbles (~2 nm or smaller) and are removed from the scatterplots by the 2 nm and 60 count cutoff. The unphysical pressures are a combination of dividing by a very small number (the radius) and with some cross-talk between Xe Lα and U minor M-series peaks at ~4.1–4.2 keV. Future work will use curve fitting of EDS idealized spectra to separate the overlap.

Overall, the bubble pressure computation is a work in progress but is very promising, and no large differences were seen in the as-irradiated vs. post-LOCA comparison here.

3. DISCUSSION

In Section 2.2, the OM characterization of the as-irradiated and post-LOCA tested state of the HBR1 rod highlights the effect that the operating conditions can have on the microstructural

evolution in the fuel and consequently its fragmentation behavior. Comparison of the OM micrographs from the NA1 and HBR1 rods in Figure 1 shows the difference in the extent of the dark zone in the fuel central regions. The dark zone in NA1 does not reach the centerline of the fuel pellet; instead, it is isolated to a ring between the mid-radius and central regions of the fuel. Conversely, the dark zone in the HBR1 sample does extend to the center of the fuel pellet, likely due to its lower last cycle power history.

The reaction that the dark zone microstructure has in response to a transient event is shown clearly in the post-LOCA micrographs in Figure 1. Both rods showed extensive fragmentation that was primarily contained within the dark zone. The fragmentation in the NA1 sample is isolated to the dark zone and does not extend to the clean fuel center unlike the HBR1 sample in which the entire center is pulverized, which can be attributed to the further penetration of the dark zone in the sample. The differences in the extent of the dark zone is believed to be at least partially dependent on temperature, where a detailed discussion of this can be found in other works [9, 14]. It appears as though the dark zone microstructure is not stable past a certain temperature after which it is currently assumed that diffusion mechanisms take over and "clean out" the microstructure. The mechanisms responsible for the formation and distribution of the dark zone remain unclear at the time of this report, but future work is planned to investigate this. The susceptibility of the dark zone to HBFF under LOCA conditions emphasizes the importance of understanding the structure's formation mechanisms.

Overall, the results in Section 2.2–2.3 show the evolution of the NA1 and NA2 samples from as-irradiated to post-LOCA states. Of particular note in Section 2.2 (Figure 1), the dark zone contrast is present in the as-irradiated and post-LOCA samples—present at around 0.5 r/r_0. From the NA1 sample, STEM results from within the dark zone (~0.53 and 0.57 r/r_0) and outside the dark zone (~0.77 r/r_0) are compared. The detailed microstructural information from STEM is currently under detailed quantification, but the general trends (i.e., Figure 9 and Figure 10) indicate that the nanostructural differences in terms of FGB size do not grossly differ inside and outside the dark zone nor between the dark and light zones. Of course, these STEM-analyzed FGBs are smaller than visible via OM, so the large (several micron) fission gas–filled bubbles will dominate the dark vs. light contrast.

The main difference between the NA1 as-irradiated and post-LOCA at the optical macrophotography level was the fragmentation of the pellet into fine particles. At the STEM level, the post-LOCA samples showed more fine-scale cavitation developing; it is likely that these small STEM-visible cavities are related to the fragmentation behavior. Transmission Kikuchi diffraction and further STEM analysis are planned to gain further insight, particularly crystallographic insight, into these behaviors.

4. FUTURE WORK

4.1 Radial Distribution of Elements Observed by Energy Dispersive X-ray Spectroscopy

An accurate correlation between the local radial burnup and the microstructures that are prone to HBFF is needed to understand the mechanisms driving HBFF. Currently, radial burnup gradients are obtained from neutronics models, but there is still some uncertainty in the generated values.

Radiochemical analysis can provide an accurate quantitative measure of the local burnup, but these methods are inherently destructive in nature and thus prevent additional microstructural characterization of the same regions. Typical radiochemical analysis is performed on a full radial cross section of fuel or even a full fuel pellet and measures the radial average burnup at a particular axial location. The axial burnup at one location can be correlated to other locations through whole pin gamma scanning. Recently, initial investigations were made to ascertain if EDS can be used to find the radial burnup gradient of a microscopy sample. This would allow local variations in burnup to be related to a segment that underwent radiochemical burnup evaluations.

Long dwell time EDS spot scan spectra were collected at 58 locations across the as-irradiated NA1 fuel sample ranging approximately 20–4215 µm from the cladding interface. These spectra were analyzed to investigate any trends that might exist in the EDS data that could be related to radial variations in burnup. Over the initial 100 µm, the point scans were collected every 5 µm after which the EDS scans were collected approximately every 100 µm. There are definite trends in the data that reflect the enhanced burnup in the periphery of the fuel, which is known to be characteristic of neutron self-shielding in a thermal neutron reactor. While this data is not as definitive as potentially quantitative electron probe microanalysis (EPMA) data, it still qualitatively reflects the expected nuclear behavior of the system.

Normalized EDS data from four different elements is visualized in Figure 14. In the figure, the radial trends in EDS signal are plotted against the distance from the fuel cladding interface in logarithmic space, which is more representative of neutron transport through a medium than linear space. For each collected spectrum, the EDS spectrum in each channel was normalized to the U M_α peak. The uranium content should remain fairly constant across the radius of the fuel pellet, and this step corrects for local variation in X-ray production. To create Figure 14, all collected EDS spectra were normalized to the 3.18 keV U M_α line to correct for local variations in uranium density. The normalized radial change in four other EDS channels are then plotted in Figure 14. The radial data is normalized to the average signal from the center of the fuel. As a check of this normalization, the signal from the 3.34 keV U $M_ß$ line (red markers) should be relatively flat, and this is reflected in the figure.

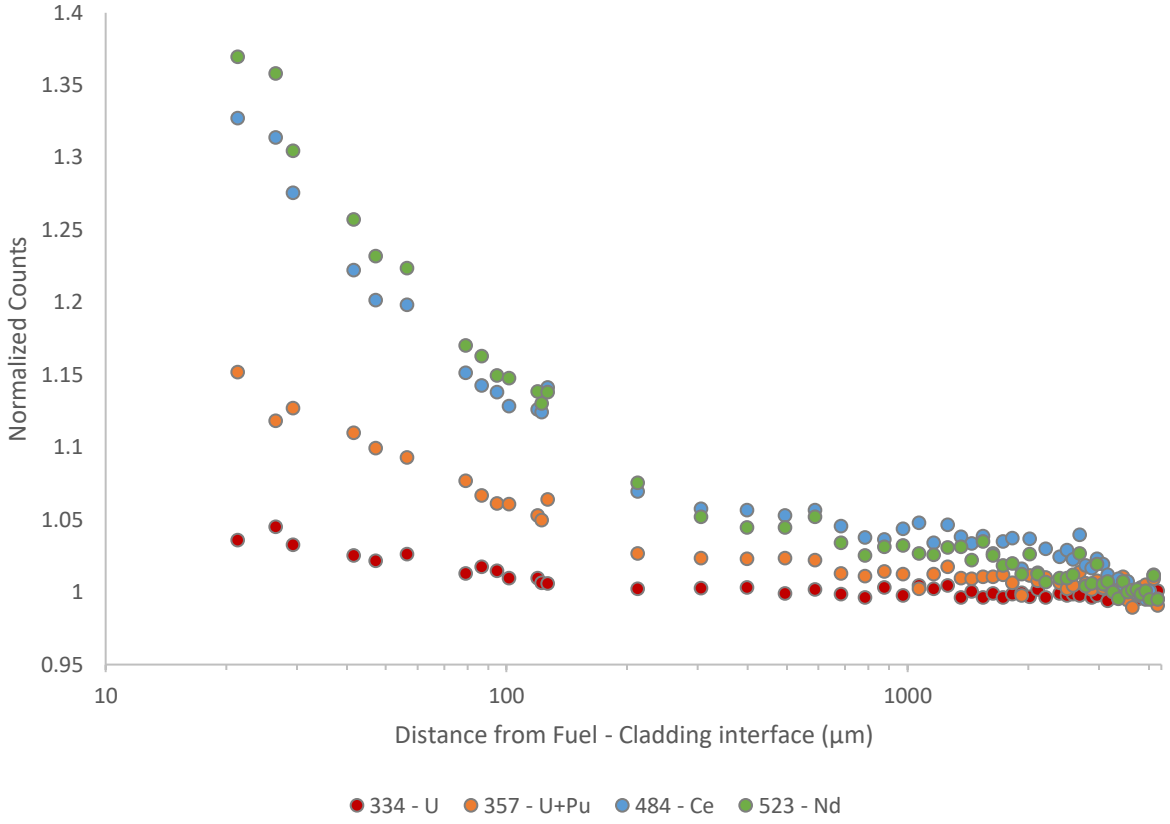

Figure 14: EDS data for different elements at different radial locations in the NA1 as-irradiated sample

In Figure 14, the signal at 3.57 keV (orange markers) is a combination of U and Pu signals from the fuel. Here the signal increase by 15% from the center of the fuel indicates an in-growth of Pu in the fuel. More interesting is the Ce (blue markers) and Nd (green markers) signals that indicate an approximate 35% increase in signal from the center of the fuel pellet. The relative Ce and Nd content is proportional to the local radial burnup in the fuel. This magnitude of change is in-line with similar observations from literature. The increase is most pronounced over the first 100 µm of fuel, where it is known that the increase in local burnup gives rise to the HBS in UO_2 fuel. Calibration of these EDS trends with radiochemical burnup evaluations of the fuel would be highly beneficial for validation of high fidelity neutronics codes in future work. This is particularly important as the correlation between local burnup and fuel fragmentation is used as a predictor of fuel performance.

4.2 Isotopic Characterization by Time-of-Flight Secondary Ion Mass Spectrometry

Time-of-flight secondary ion mass spectrometry (ToF-SIMS) is a powerful tool that enables the characterization of the spatially resolved isotopic composition of a sample in addition to chemical information. Traditionally, it is performed with a stand-alone instrument, but with recent advances in the techniques that can be performed in electron microscopes, ToF-SIMS can

now be accomplished by collecting the ions of the elements (or molecules) being ionized by a FIB beam. The use of a gallium FIB beam does result in a large peak in the spectra at 69 m/Q—seen in Figure 15(a) and Figure 15(b)—due to the collection of the Ga ions that are used to bombard the sample, but this is straightforward to identify and filter out as long as there is certainty that gallium is not in the sample. Due to the novelty of the technique being used in conjunction with a FIB on these irradiated samples, there is currently some doubt regarding the quantitative certainty of the data, but it is still capable of providing a good qualitative analysis of the sample.

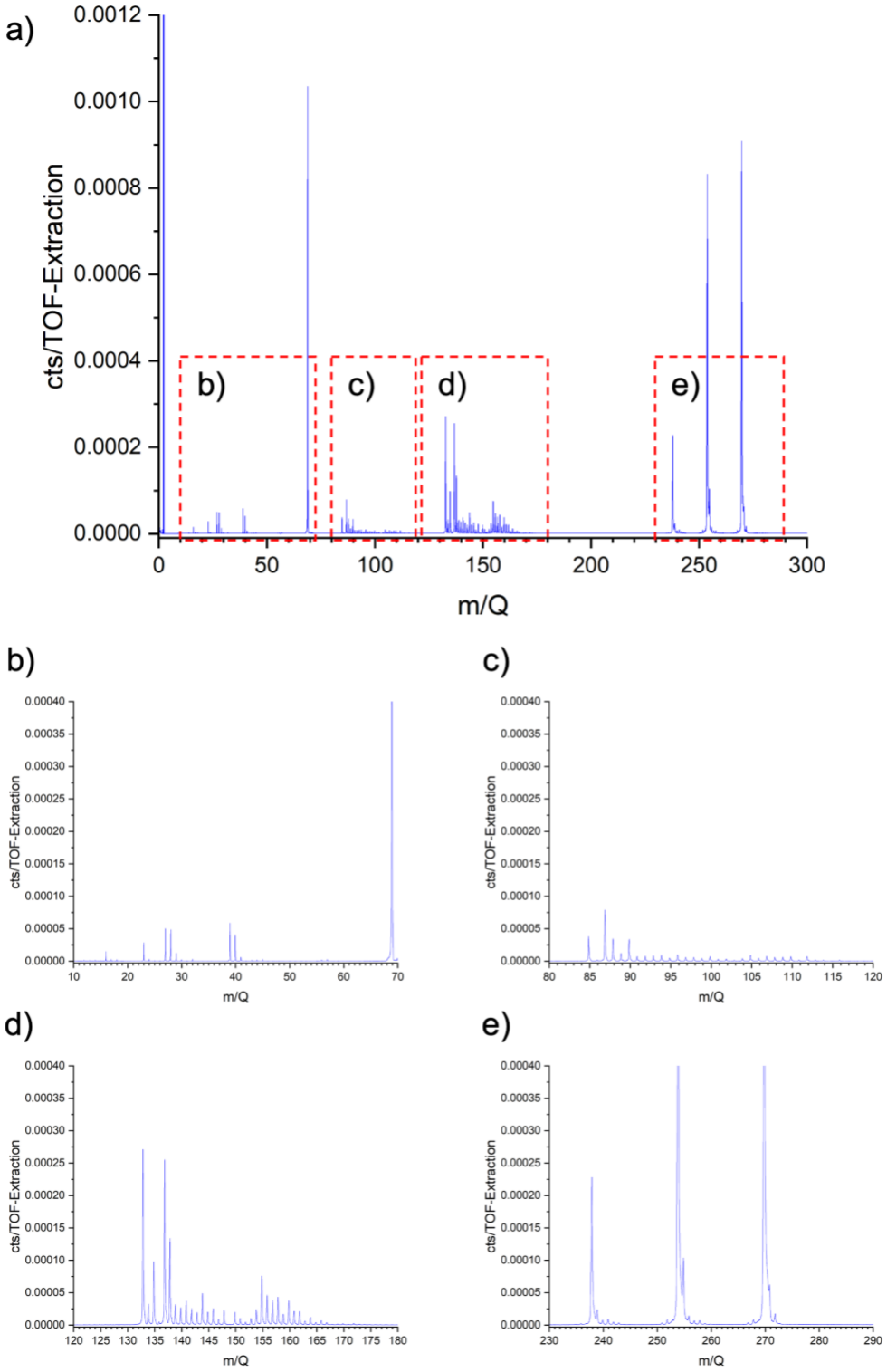

Figure 15: ToF-SIMS spectra obtained from the HBS in the NA1 as-irradiated sample. (a) Provides the entire spectra collected from 0–300 m/Q. (b)–(e) Show portions of the spectra to highlight the distribution of the individual peaks.

In Figure 15(a), the spectra between 0 and 300 m/Q—where *m/Q* represents the mass-to-charge ratio—obtained from the HBS of the NA1 as-irradiated fuel segment is given. The cropped spectra in Figure 15(b)–(e) allow for the different peaks to be distinguished in the selected ranges. Various fission products from the lower and upper mass fission product distributions can be seen in Figure 15(c) and (d) respectively. The lower mass fission products do not include Kr isotopes. The signal at 85 m/Q is likely due to Rb-85, not Kr-85, since the more abundant krypton isotopes Kr-84 and Kr-86 masses are not present in the data. Signal at m/Q 87 to 90 are likely from Sr isotopes. The signal between 91 and 110 are likely various stable isotopes of Zr, Nb, Mo, Ru, Rh, and Pd. The higher mass fission product signals from 133 to 165 are mostly from stable lanthanide fission products and their oxides. Another point that is interesting to note when viewing the spectra are the peaks at 238, 254, and 270. The first can be attributed to U-238, while the second and third are also U-238 with either one or two O-16 attached. This can make the analysis challenging when trying to determine whether the collected peak is from a single element, a molecule, or possibly both. Currently, this technique is still relatively new to fuels characterization, and work is needed to increase the confidence and aid in the interpretation of the data that is collected. To address this, more work is planned on fabricated samples of UO_2 where the isotopic composition is known so that the comparison can be made between the known composition and what is measured by the ToF-SIMS.

5. SUMMARY

This work presented the results from a multiscale characterization effort that utilized OM and S/TEM to understand the mechanisms driving HBFF. Two rods of commercial high burnup LWR UO_2 with different power histories were compared in the as-irradiated and post-LOCA tested state with OM. The OM results showed the susceptibility of the dark zone in the fuel center to HBFF, and work is ongoing to uncover the mechanisms behind this structure's formation. S/TEM analysis did not uncover large differences at the nanoscale between the dark zone and light zone in the as-irradiated samples that might indicate why the structure is prone to HBFF. However, comparison between as-irradiated and post-LOCA tested samples showed the increase of nanoscale bubbles in the post-LOCA samples that may be related to fragmentation behavior. Further characterization is needed to gain crystallographic insight that will enable a better understanding of the nanoscale FGB behavior.

6. ACKNOWLEDGMENTS

This work was supported by the US Department of Energy Office of Nuclear Energy, Advanced Fuels Campaign under contract DE-AC05-00OR22725 with UT-Battelle LLC.

7. REFERENCES

[1] W. Wiesenack, "Summary of the Halden project LOCA test series IFA-650," in "HPR-380, OECD NEA Halden Reactor Project," 2013.

[2] L. Kekkonen, "LOCA testing in Halder, the Fourth Experiment: IFA-650.4," in "HWR-838, Halden Reactor Project," 2007.

[3] B. Oberlander, M. Espeland, and N. Solum, "PIE results from the high burnup (92 GWd/MTU) PWR segment after LOCA testing in IFA 650-4," in *Proc. of the EHPG Meeting*, 2011.

[4] N. Capps *et al.*, "A critical review of high burnup fuel fragmentation, relocation, and dispersal under loss-of-coolant accident conditions," *Journal of Nuclear Materials*, vol. 546, p. 152750, 2021.

[5] N. Capps, R. Sweet, J. Harp, and C. M. Petrie, "High-burnup fuel stress analysis prior to and during a LOCA transient," *Journal of Nuclear Materials*, vol. 556, p. 153194, 2021.

[6] I. Zacharie-Aubrun, R. Dowek, J. Noirot, T. Blay, M. Cabié, and M. Dumont, "Restructuring in high burn-up UO2 fuels: Experimental characterization by electron backscattered diffraction," *Journal of Applied Physics*, vol. 132, no. 19, p. 195903, 2022.

[7] R. L. Seibert, J. W. Werden, C. M. Parish, J. M. Harp, T. J. Gerczak, and N. A. Capps, "Initial Microstructure Examination of High Burnup Fuel with Varying Operational Burnups," Oak Ridge National Laboratory, Oak Ridge, TN, ORNL/SPR-2022/2503, 2022.

[8] R. Seibert *et al.*, "Advanced Microscopy Characterization of High Burnup Commercial UO2 Fuel Before and After LOCA Testing," Oak Ridge National Laboratory, Oak Ridge, TN, ORNL/SPR-2022/2618, 2022.

[9] C. McKinney *et al.*, "Characterization of the Radial Microstructural Evolution in LWR UO2 Using Electron Backscatter Diffraction☆," *Journal of Nuclear Materials*, p. 154605, 2023.

[10] T. J. Gerczak, C. M. Parish, P. D. Edmondson, C. A. Baldwin, and K. A. Terrani, "Restructuring in high burnup UO2 studied using modern electron microscopy," *Journal of Nuclear Materials*, vol. 509, pp. 245-259, 2018/10// 2018, doi: 10.1016/j.jnucmat.2018.05.077.

[11] D. Jadernas and D. Wachs, "Sample Selection Report for the Irradiation and Post Irradiation Examination of Ultra High Burn up Fuel," Idaho National Lab.(INL), Idaho Falls, ID (United States), INL/EXT-17-44054, 2018. [Online]. Available: https://doi.org/10.2172/1466834. https://www.osti.gov/servlets/purl/1466834

[12] C. M. Parish, "When Will Low-Contrast Features be Visible in a STEM X-ray Spectrum Image?," presented at the Microscopy and Microanalysis, 2015.

[13] L. Yang and B. Wirth, "An improved xenon equation of state for nanobubbles in UO2," *Journal of Nuclear Materials*, vol. 572, p. 154089, 2022.

[14] F. Cappia *et al.*, "Detailed characterization of a PWR fuel rod at high burnup in support of LOCA testing," *Journal of Nuclear Materials*, vol. 569, p. 153881, 2022.